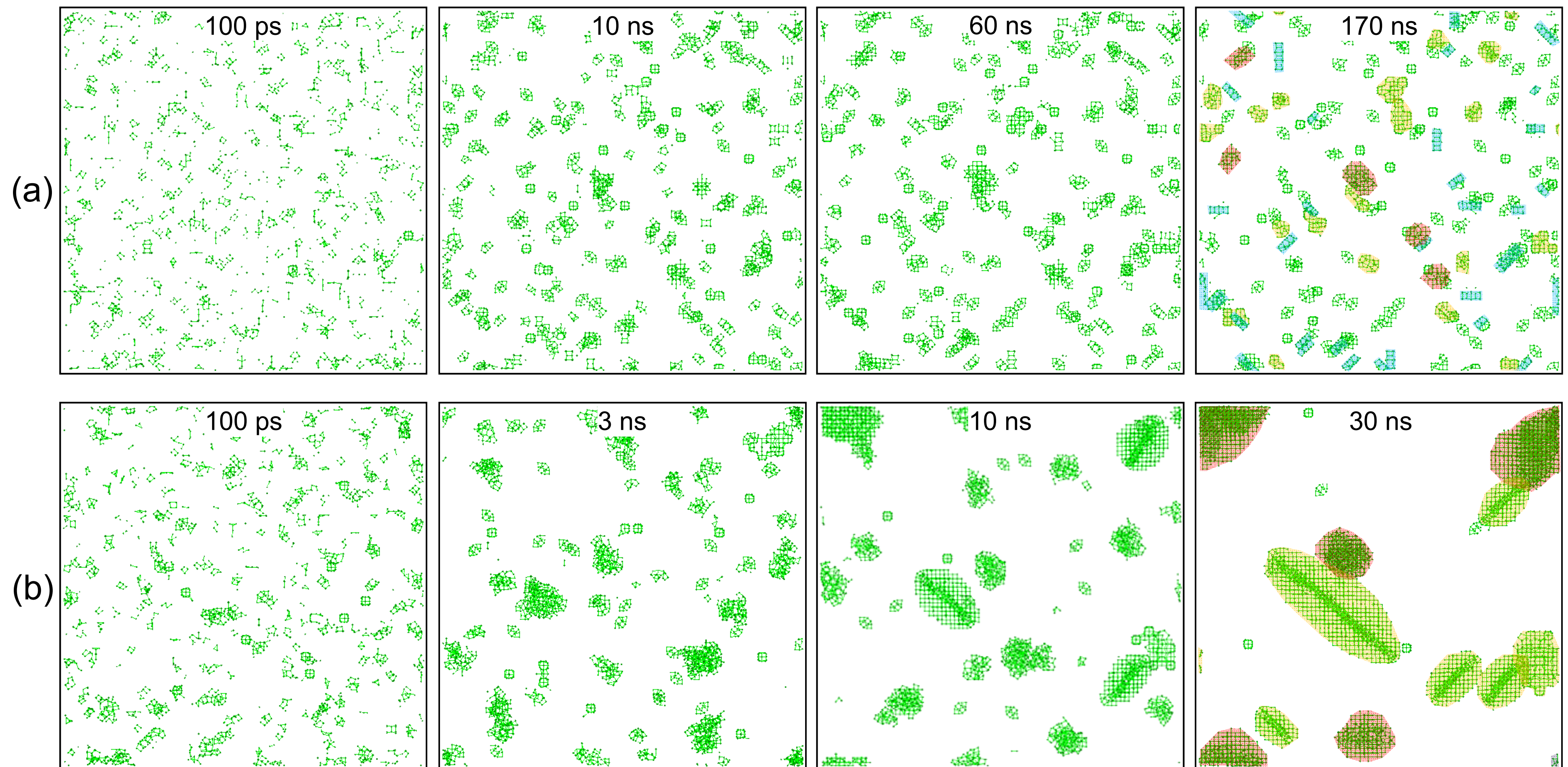

Figure 1. ZY projections of the DAs within the simulation cell taken during annealing at (a) $T^* = 0.50$, and (b) $T^* = 0.79$. Corresponding times, measured from the start of each MD simulation, are shown on every snapshot. In (a) clusters shadowed in red are {111} rod-like defects, in blue are <011> chains, and in yellow small agglomerates of tetra-$\mathcal{I}$s. In (b) {001} loops are shadowed in yellow and {111} dislocations are shadowed in red. In (a) $\mathcal{I}$ aggregation proceeds by Ostwald ripening, while in (b) it is a consequence of the coalescence of highly-mobile liquid droplets that spontaneously transform into {001} loops when certain size is reached. It is worth to note that these loops produce strong strain fields around them: atoms above and below the defect planes are in perfect tetrahedral positions, but they are shown as DAs in the last snapshot of (b) because they have been pulled far from regular lattice sites due to the stress created by the layers where $\mathcal{I}$s lie.

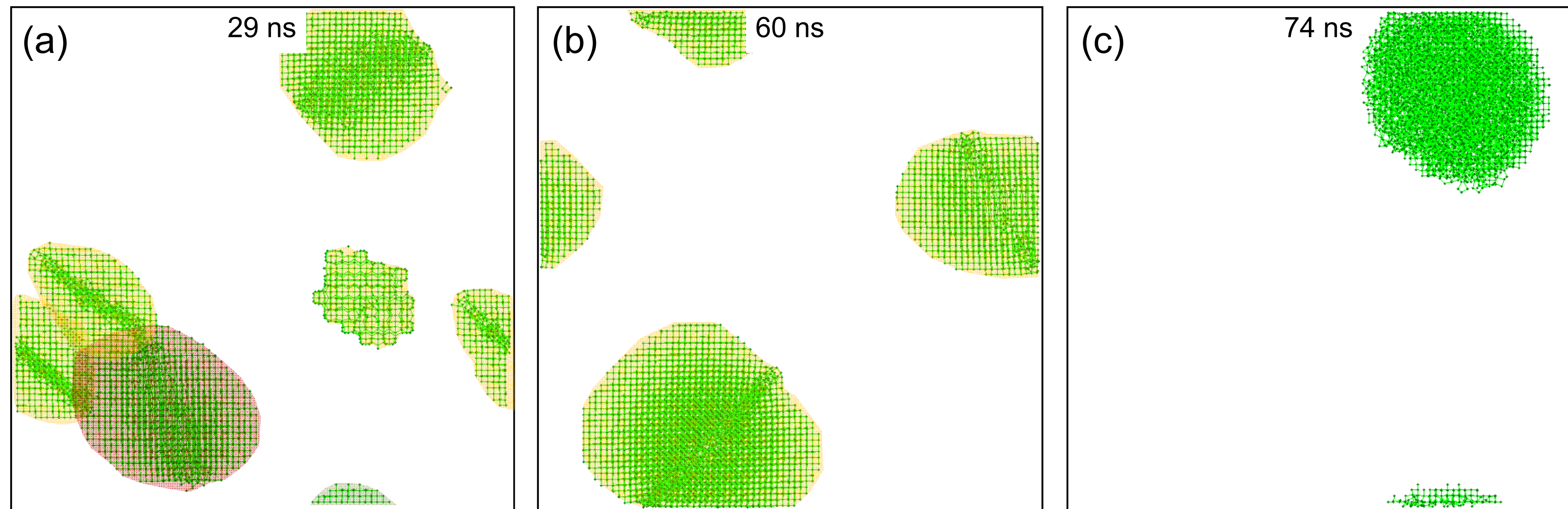

Figure 2. ZY projection of the DAs within the simulation cells after annealing for: (a) 29 ns at $T^* = 0.83$, (b) 60 ns at $T^* = 0.88$, and (d) 74 ns at $T^* = 0.92$. Extended defects shadowed in yellow are {001} loops and dislocations, while {111} dislocations are shadowed in red. The only remaining $\mathcal{I}$ defect shown in (c) shows no ordered structure, and encompasses all $\mathcal{I}$s initially introduced in the lattice.

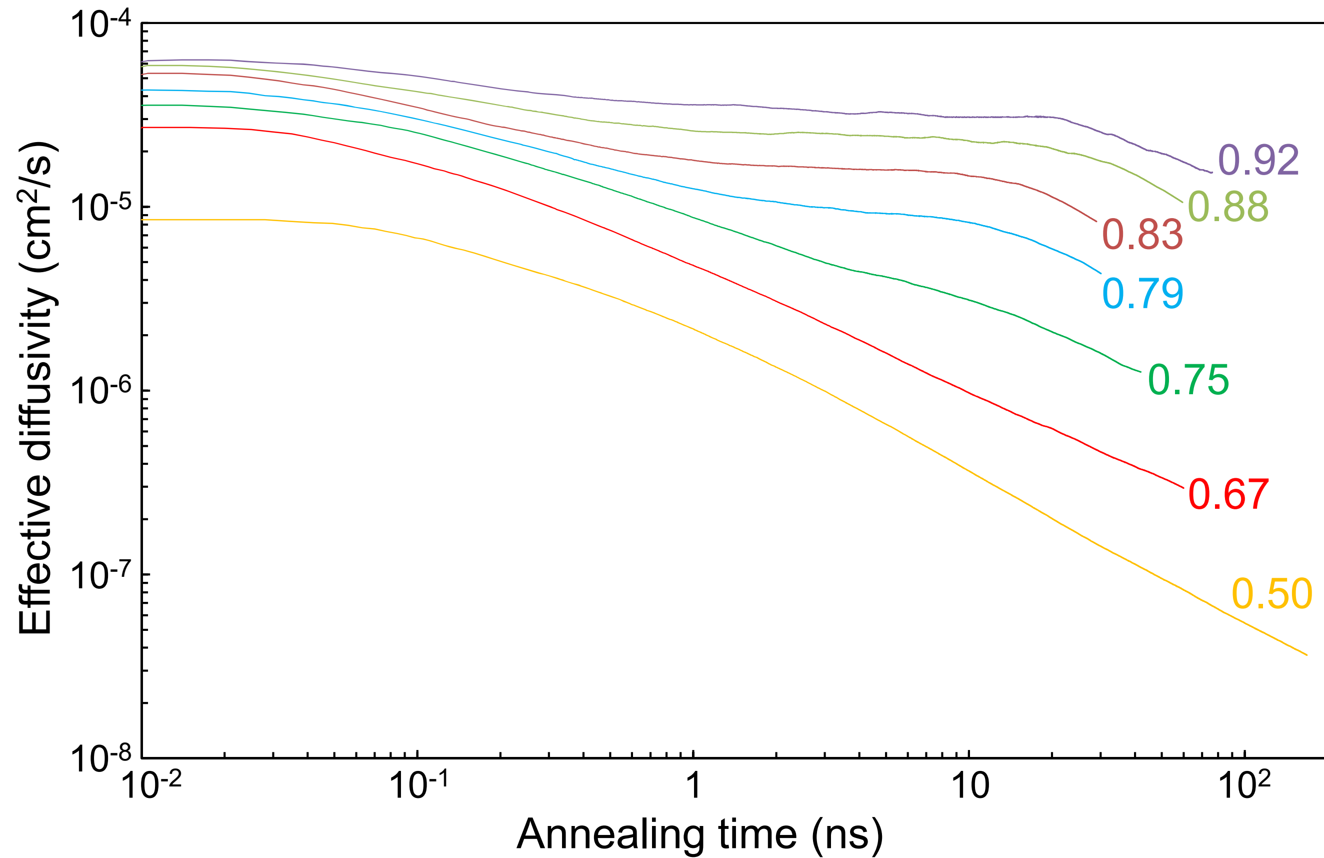

Figure 3. Effective diffusivities as a function of time during annealing at several reduced temperatures. For low temperatures we see an initial plateau corresponding to the weighted average diffusivity of highly-mobile species (single ℐs, di-ℐs and tri-ℐs) followed by a dependence close to 1/time indicative of a halted diffusion when mobile ℐs become trapped in stable immobile clusters. At higher temperatures we notice an additional plateau at intermediate times revealing the onset of other mobile species, i.e., the liquid-like ℐ-rich clusters, which turn again into a dependence 1/time when these disordered clusters transform into immobile {001} loops. Effective diffusivities ($\geq 10^{-5}$ cm^2/s) of these liquid droplets are lower but comparable to those corresponding to the highly-mobile species present at the early stages of the simulations.

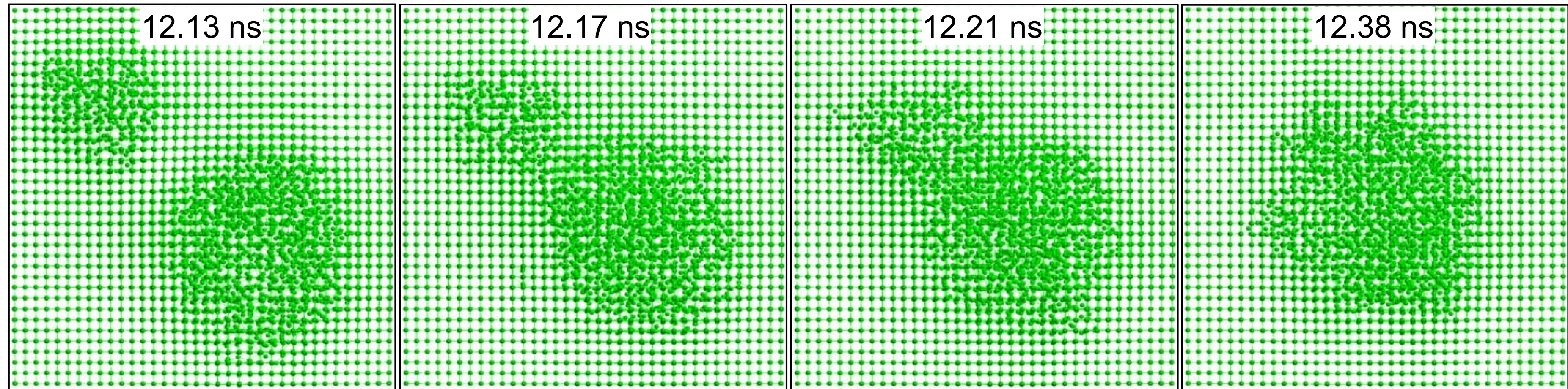

Figure 4. ZY views showing the coalescence of two ℐ-pockets during annealing at $T^* = 0.88$, where times are measured from the start of the MD simulation. Initial pockets have 70 ℐs and 241 DAs, and 256 ℐs and 1135 DAs, respectively, while final pocket have 326 ℐs and 1527 DAs. This final pocket has been used to calculate the pair distribution function that appears in manuscript Fig. 2.

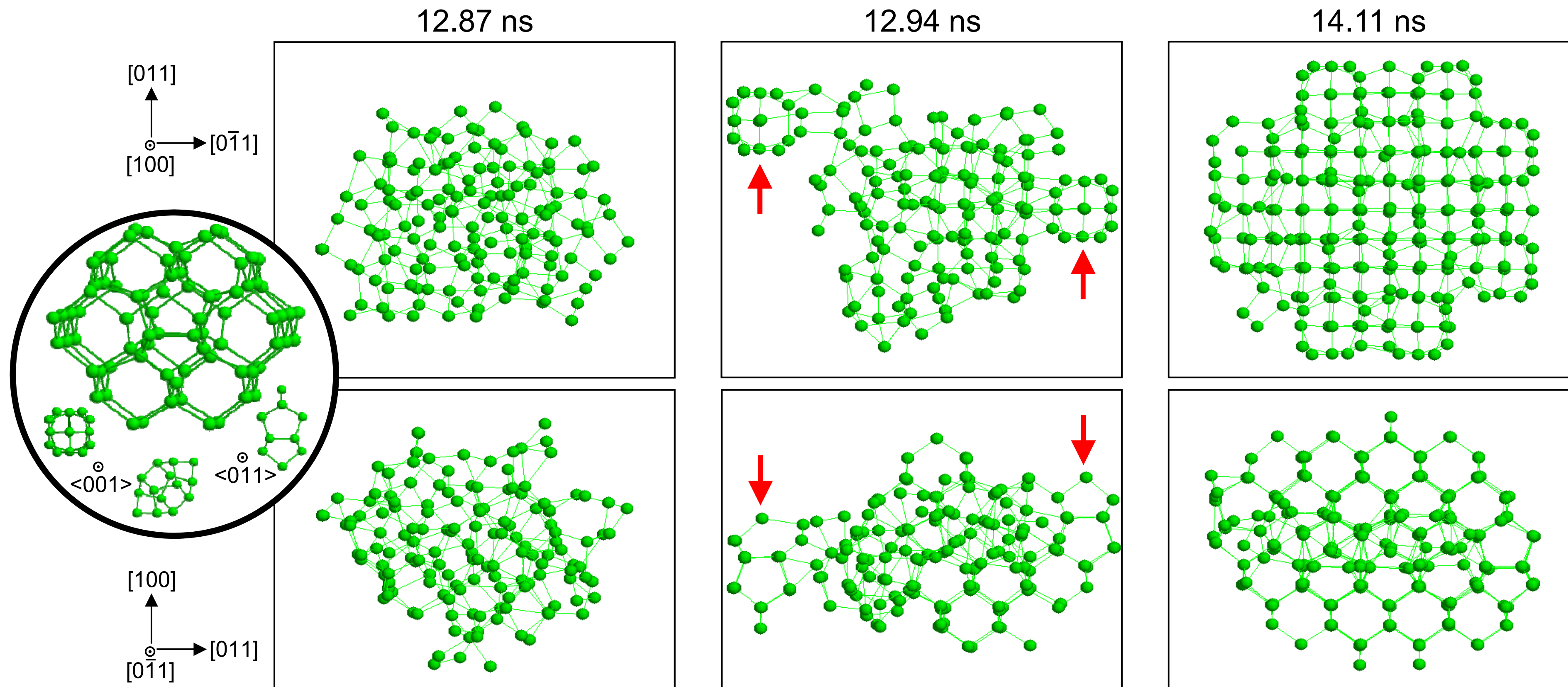

Figure 5. Snapshots taken from the sample annealed at T^* = 0.79 depicting the formation of {001} loops (only DAs are shown). Times are measured from the start of the simulation. Upper snapshots correspond to top views, and bottom snapshots with side views. Arrows indicate the Arai tetra-$\mathcal{I}$ that nucleate in the $\mathcal{I}$-defect edges. Inset on the left shows the atomic configuration of the Arai tetra-$\mathcal{I}$, along with different views of this defect when displaying only the DAs.

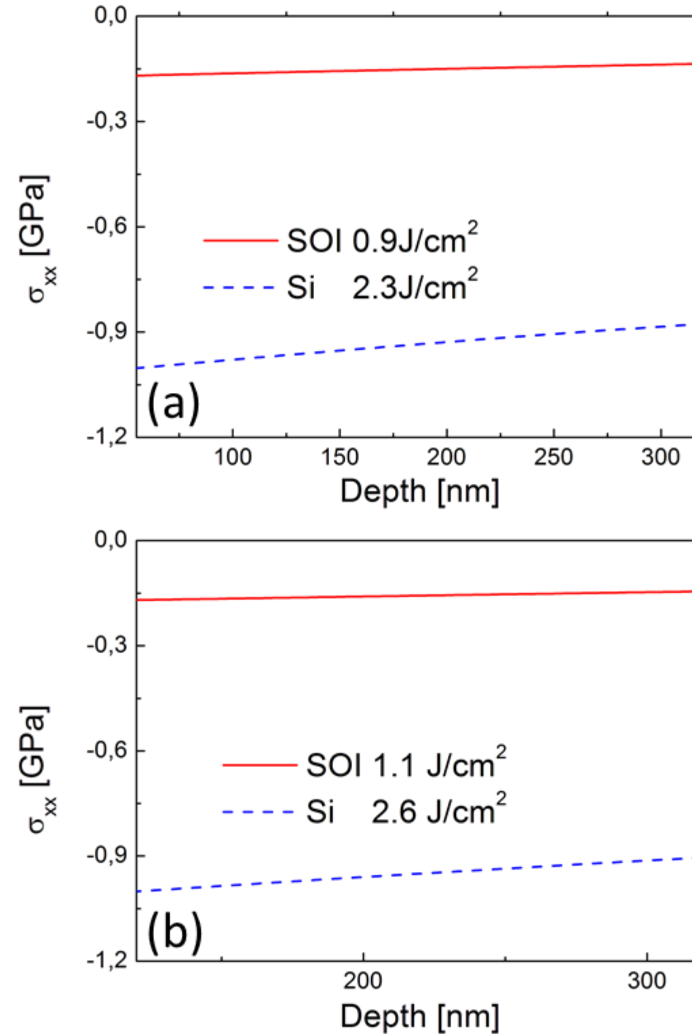

Figure 6. Maximum local stress field calculated with the thermo-elastic theory in the solid region below the maximum melt depth position for LA processes promoting similar melt depth extensions [~55 nm panel (a) and ~110 nm panel (b)] in bulk Si and SOI samples. The constitutive relations $\sigma_{ij} = \mathbf{E}[\varepsilon_{kl} - \alpha\delta_{kl}(T - T_0)]$, relating the stress σ, strain ε, and thermal fields, are calibrated with the c-Si and SiO_2 elastic constants tensor **E** and expansion coefficient α. Here, zero stress conditions are imposed for the stress components σ_{zz} normal to the free boundary (i.e., the free surface or the liquid/solid interface). Moreover, the continuity of the strain components ε_{zz} is also imposed at the interface between different material regions.

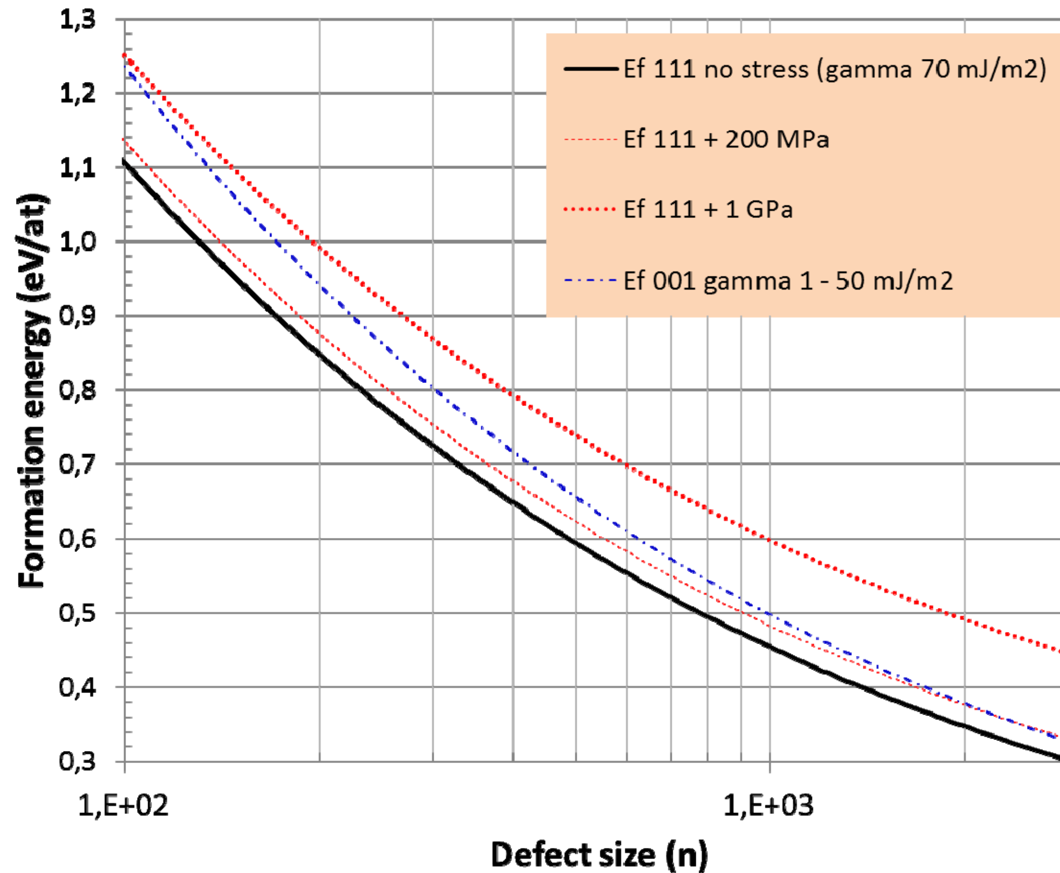

Figure 7. Formation energy of conventional {111} (black solid line) and "unconventional" {001} (blue dash-dotted line) dislocation loops as a function of defect size (number of ℐs contained in the loop) in the absence of an external stress field. The upper limit of the stress field developed during laser annealing is different depending on the substrate type: ~ -1 GPa for bulk Si and ~ -0.2 GPa for SOI (cf. previous figure). This stress field does not modify the formation energy of the {001} loops (their Burgers vector is perpendicular to the stress plane). In contrast, when calculated in the presence of the external stress, the formation energy of {111} loops strongly increases and overcomes that of {001} loops in the Si case (thick red dotted line), whereas it remains lower than that of {111} loops in the SOI case (thin red dashed line). As a consequence, the inversion of the stability from {111} to {001} defects, predicted in the reference Si case, is not expected in SOI. However, in spite of the unfavorable energetic argument, {001} dislocation loops are formed in the SOI substrate, similarly to the Si reference case.

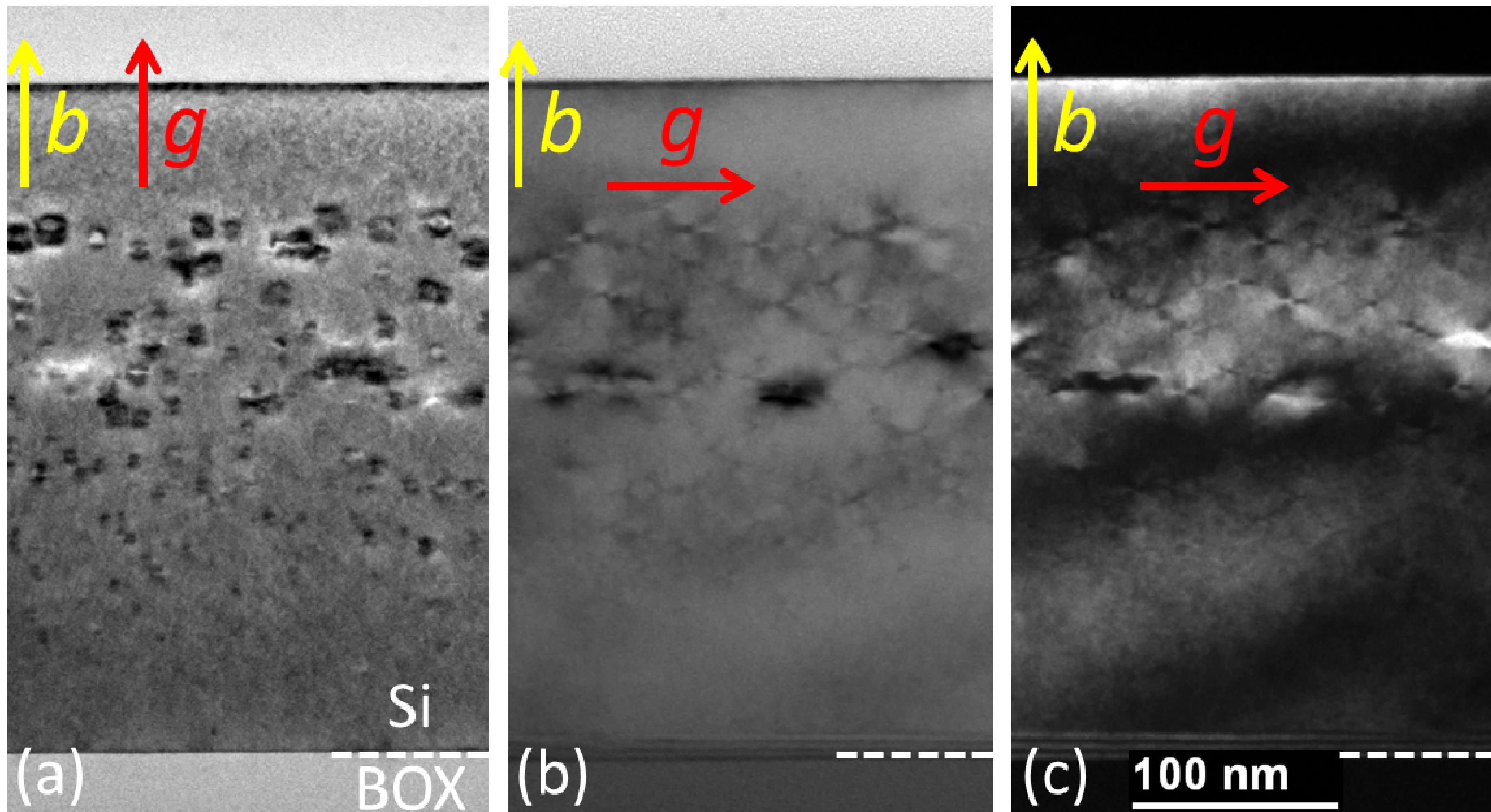

Figure 8. Cross-section TEM images from the SOI substrate annealed at 0.9 J/cm^2. All images are taken using the [1 -1 0] zone axis and different diffracting vectors ***g***. (a): ***g*** = [0 0 4]. In this case, the loop Burgers vector ***b*** [0 0 1] is parallel to ***g*** resulting in maximum defect contrast. (b) and (c): ***g*** = [2 2 0], respectively in bright field (b) and weak-beam dark field (c) conditions. In (b) and (c), the loop Burgers vector ***b*** [0 0 1] is perpendicular to ***g*** resulting in vanishing contrast (***g.b*** = 0).

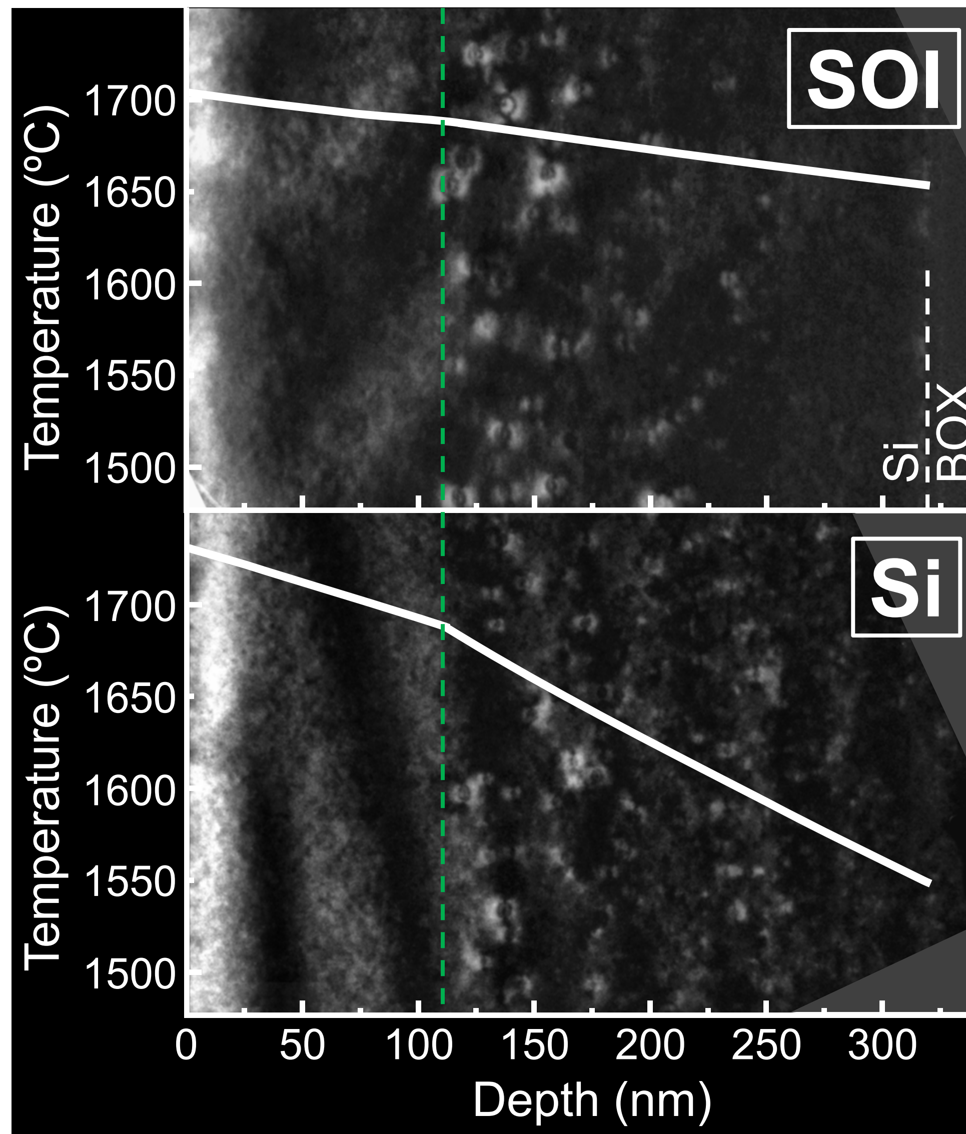

Figure 9. Cross-section TEM micrographs from the SOI substrate annealed at 1.1 J/cm^2, and the bulk Si substrate annealed at 2.6 J/cm^2. Superimposed are the corresponding local maximum temperature depth profiles, calculated by phase-field simulations. These laser anneal conditions result in similar melt depths within the two different substrates, as indicated by the green dashed line.